



Article

A Time–Frequency Composite Recurrence Plots-Based Series Arc Fault Detection Method for Photovoltaic Systems with Different Operating Conditions

Zhendong Yin ¹, Hongxia Ouyang ¹, Junchi Lu ¹, Li Wang ² and Shanshui Yang ^{2,*}

¹ College of Electrical, Energy and Power Engineering, Yangzhou University, Yangzhou 225127, China; zdyin@yzu.edu.cn (Z.Y.); mz120241266@stu.yzu.edu.cn (H.O.); mz120241253@stu.yzu.edu.cn (J.L.)

² Department of Electrical Engineering, Nanjing University of Aeronautics and Astronautics, Nanjing 211106, China; liwang@nuaa.edu.cn

* Correspondence: yshanshui@nuaa.edu.cn

Abstract: Series arc faults (SAFs) pose a significant threat to the safety of photovoltaic (PV) systems. However, the complex operating conditions of PV systems make accurate SAF detection challenging. To tackle this issue, this article proposes a SAF detection method based on time–frequency composite recurrence plots (TFCRPs). Initially, variational mode decomposition (VMD) is employed to decompose the current into distinct modes. Subsequently, the proposed TFCRP transforms these modes into two-dimensional matrices, enabling the measurement of composite similarity between different phase states. Lastly, extra tree (ET) is utilized to fuse the fractional recurrence entropy (FRE) and the singular values extracted from the matrices, thereby achieving SAF detection. Experimental results indicate that the proposed method achieves a detection accuracy of 98.75% and can accurately detect SAFs under various operating conditions. Comparisons with different methods further highlight the advancement of the proposed method. Furthermore, the detection time of the proposed method (209 ms) meets the requirements of standard UL1699B.

Keywords: arc fault; variational mode decomposition; time–frequency composite recurrence plots; fractional recurrence entropy; singular value decomposition; extra tree



Academic Editors: José de Jesús Rangel Magdaleno and Oscar Martínez-Fuentes

Received: 25 November 2024

Revised: 4 January 2025

Accepted: 6 January 2025

Published: 8 January 2025

Citation: Yin, Z.; Ouyang, H.; Lu, J.; Wang, L.; Yang, S. A Time–Frequency Composite Recurrence Plots-Based Series Arc Fault Detection Method for Photovoltaic Systems with Different Operating Conditions. *Fractal Fract.* **2025**, *9*, 33. <https://doi.org/10.3390/fractalfract9010033>

Copyright: © 2025 by the authors. Licensee MDPI, Basel, Switzerland. This article is an open access article distributed under the terms and conditions of the Creative Commons Attribution (CC BY) license (<https://creativecommons.org/licenses/by/4.0/>).

1. Introduction

Given the escalating concerns surrounding the greenhouse effect and resource depletion, there is an urgent need to identify viable alternatives to fossil fuels in order to satisfy the growing electricity demands of human society. Consequently, all nations are prioritizing the development of renewable energy sources and striving to transition towards a low-carbon energy structure. Photovoltaic (PV) energy, with its abundant reserves and significant development potential, has garnered increasing attention for its exploitation and utilization [1]. The global installed capacity of PVs is projected to reach 375 GW by 2024, marking a year-on-year increase of 31.8% in total installed capacity.

PV systems are composed of numerous cables and terminals. Over time, external stressors such as high temperatures, humidity, and wear can lead to insulation damage in cables or loose connection terminals, posing a risk of arc faults. The temperature at the site of an arc fault can escalate to 3000 °C, making it prone to igniting nearby combustible materials and triggering a fire. Arc faults can result in substantial property damage, and the extensive pollutants emitted by fires can contaminate the air. Furthermore, the shutdown of PV power generation systems due to arc faults reduces the supply of renewable energy.

Thus, arc faults can have severe negative impacts on both the environment and the economy. Among these, series arc faults (SAFs) pose a significant threat to the safety and stability of PV systems. SAFs represent an unstable plasma state that can cause a slight decrease in line current [2], making them difficult to detect using traditional protective devices. Effectively implementing SAF detection remains a highly challenging issue.

SAF detection can be achieved through the analysis of sound signals, light signals, thermal signals, and electromagnetic radiation signals. However, these detection methods rely on the external physical characteristics of SAFs and require the detection device to be installed near the fault location. Unfortunately, the location of SAFs in practical systems is highly uncertain. Therefore, the detection method based on the external physical characteristics of arc faults is only suitable for systems with limited spaces [3].

The SAF detection methods based on current signals have garnered increasing attention. Some scholars have implemented SAF detection using thresholds derived from extracted capacitance voltage peaks [4], frequency domain energy [5], and autocorrelation values [6]. However, practical systems often exhibit multiple working states, leading to significant variations in the single features extracted under different operating conditions. Consequently, determining an appropriate threshold for a single feature in a practical system to accommodate different working states becomes challenging [7]. Currently, a growing number of scholars are exploring the application of machine learning to fuse various types of features for arc fault detection with the aim of enhancing the adaptability of detection methods. In [8], the arc current signal was processed using empirical mode decomposition (EMD) for noise reduction, and the extracted features (energy, Shannon entropy, root mean square, and standard deviation) were input into a support vector machine (SVM) to obtain detection results. In [9], a high-dimensional feature vector was constructed by extracting the crest factor, correlation coefficient, harmonic values, and wavelet packet entropy from the arc current. Feature selection based on random forests (RFs) was applied to reduce the interference of low-contribution features on the detection results. In [10], different components of the current signal were obtained using the improved empirical wavelet transform, and weight energy entropy, sample entropy, and the root mean square value were extracted to construct a feature vector. This feature vector was then processed by an extreme learning machine to produce the detection results. In [11], to avoid the subjectivity of manually extracting features, abstract fault features in the current signal were directly mined using a 1D convolutional neural network.

Machine learning algorithms are complex, and the time costs and hardware costs of training machine learning algorithms are higher than those of traditional threshold methods. Moreover, the performance of machine learning algorithms depends on the quality of the data, and how to further enhance the generalization ability of machine learning algorithms is currently an important research topic in the field of artificial intelligence. However, it cannot be ignored that the SAF detection methods based on machine learning can effectively enhance adaptability compared to those based on single feature threshold.

However, previous studies have primarily focused on extracting features directly from one-dimensional current signals. Converting these one-dimensional signals into two-dimensional matrices can enhance the structural information of the signals, making it easier to extract subtle fault information [12]. The method of converting one-dimensional signals into two-dimensional matrices has been successfully applied in the field of fault diagnosis and has achieved promising results [13]. The time–frequency matrix obtained based on the generalized S-transform can accurately reflect the local characteristics of frequency components over time [14]. SAF detection results can be obtained by inputting the energy features extracted from the time–frequency matrix into an SVM. In [15], the arc current signal was transformed into a two-dimensional matrix using the truncated matrix

construction method, and singular values extracted from the matrix were used as features to achieve SAF detection. Compared to traditional Hankel matrices, truncated matrices not only have a faster construction speed but also can preserve fault information completely. In [16], short-time Fourier transformation was utilized to convert the one-dimensional arc current signal into a two-dimensional time–frequency matrix, effectively encapsulating the spectral features that contain crucial fault information. In [17], the data of the same time window of voltage and current at different positions of the system were fused into a matrix, and the key components in the matrix were extracted as fault characteristics based on principal component analysis. The time–frequency matrix can be obtained by using fractional Fourier transform to analyze arc current signals in the rotating time–frequency plane [18]. Singular values of different levels of the time–frequency matrix can be extracted as fault features based on two-level block singular value decomposition, and accurate detection results can be obtained based on an SVM. Converting an arc current into a two-dimensional matrix can improve the performance of SAF detection, but it is still necessary to explore more effective matrix conversion methods to overcome the interference of complex transient working states of the systems, which is one of the motivations of this article.

Recurrence plots (RPs) are an excellent matrix conversion method, and the matrix obtained based on RPs includes many signatures of the arc current that cannot easily be extracted by other tools [3]. In [19], unthresholded recurrence plots were applied to solve the problem that the matrix obtained based on traditional RPs being prone to losing the subtle similarity information of arc currents. At the same time, texture features and singular values extracted from the IRP-based matrix are input into a neural network to obtain SAF detection results. Some scholars integrated the idea of multi-scale into RPs [20], which can extract more abundant fault information than using a single scale, thus helping to improve the accuracy of time series classification. In [21], cross-recurrence plots were proposed to integrate the similarity information between vibration signals at different locations in the bearing system, thus facilitating the improvement of fault diagnosis performance. However, RPs and their improved forms have the following shortcomings: (1) the adoption of Euclidean distance as a single similarity evaluation index lacks the ability to comprehensively reveal the similarity between different states in phase space; (2) the dynamic characteristics of time series can only be analyzed from the time domain, and the critical fault information hidden in the frequency domain cannot be fully utilized. Moreover, how to effectively extract fault features from RPs is an important aspect to ensure accurate SAF detection.

This article intends to excavate the rich texture information hidden in arc currents based on RP theory. In this paper, a novel TFCRP is proposed. The TFCRP can overcome the deficiency of traditional RPs, namely that the similarity analysis tool is too simple and the critical fault information in the frequency domain cannot be mined. In addition, the TFCRP solves the limitation of the traditional matrix conversion-based SAF detection method being unable to mine time–frequency similarity signatures. A SAF detection framework, integrating VMD, a TFCRP, FRE, singular value decomposition (SVD), and ET, is illustrated in Figure 1. The contributions of this paper encompass the following four key aspects:

(1) To address the limitation of the similarity analysis method in traditional RP, a composite similarity analysis method is proposed in the TFCRP. The proposed composite similarity analysis method not only calculates the Euclidean distance between distinct states in the phase space but also evaluates the directional similarity of these states based on cosine distance. Additionally, it achieves a fusion of Euclidean distance and cosine distances through a weighting factor;

(2) To surpass the limitation of the traditional RP's inability to analyze fault information in the frequency domain, the TFCRP proposes a method for examining the similarity

of dynamic frequency domain energy states. Firstly, the arc current is decomposed into different modes and a time–frequency energy state matrix is constructed. Then, the composite similarity between frequency domain energy states at different time instants is calculated. Finally, based on the RP concept, the extraction of fault information in the frequency domain is innovatively realized;

(3) In this paper, SVD and FRE are used to extract features from the matrix obtained from the TFCRP. The novel FRE is proposed to measure the complexity of recurrence plots obtained from the TFCRP at different fractional orders. In contrast to the extraction of traditional single-order recurrence entropy (RE), extracting FRE as fault features can enhance the diversity of fault information, and the advantages of fault information of different orders vary under different circumstances;

(4) This article validates the proposed SAF detection method under the diverse operating conditions of PV systems and compares the proposed method with existing SAF detection methods to demonstrate its advancement. Experimental results show that the detection accuracy of the proposed method can reach 98.75%. Compared to other methods, it more effectively mitigates the interference of changing working conditions on detection results. Furthermore, the precision (98.39%), recall (99.18%), and F1 score (98.78%) of the proposed method is higher than that of the other eight methods, which indicates that the proposed method excels at suppressing false alarms.

The structure of this article is organized as follows: Section 2 introduces the basic principles of VMD; Section 3 elaborates on the proposed TFCRP; Sections 4 and 5 present the details of SVD and ET, respectively; Section 6 presents the experimental data collection; Section 7 analyzes the experimental results; and Section 8 concludes this article.

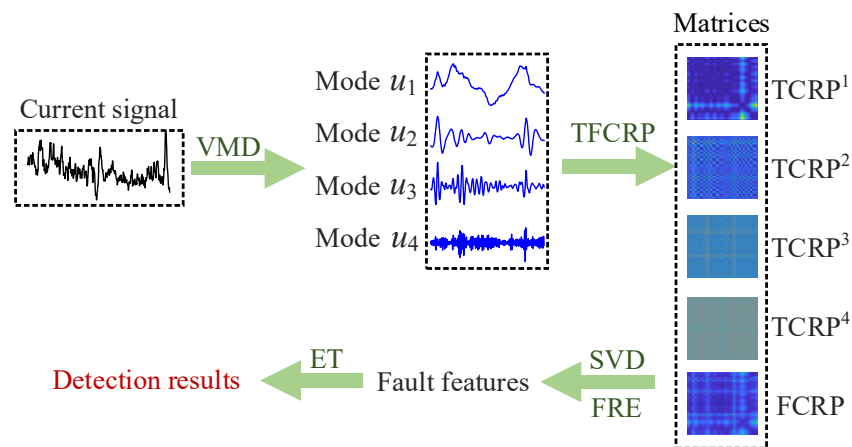


Figure 1. The framework of the proposed SAF detection method.

2. Variational Mode Decomposition

VMD achieves the extraction, recovery, and combination of signal modes using a recursive method [22] which adaptively divides the spectrum of the input signal. Compared to EMD, VMD boasts a comprehensive mathematical foundation. Additionally, VMD effectively mitigates the non-stationarity of signals, facilitating a more precise extraction of arc fault features.

If the arc current signal input into VMD is $F(t) = \{x_t | t = 1, 2, \dots, n\}$, x_t is the t -th point of $F(t)$. VMD needs to solve the constrained variational problem, as shown in Equation (1).

$$\min_{\{u_k\}, \{\omega_k\}} \sum_{k=1}^K \left\| \partial_t \left[\left(\delta(t) + \frac{j}{\pi t} \right) * v_k(t) \right] e^{-j\omega_k t} \right\|_2^2 \quad (1)$$

$$s.t. \sum_k v_k(t) = F(t)$$

where K is the number of modes obtained after decomposition. $\{v_k\}$ represents the k -th mode. $\{\omega_k\}$ is the center frequency of the k -th mode. $\delta(t)$ and $*$ denote the dirac delta function and convolution operation, respectively.

By introducing the Lagrange multiplication factor and quadratic penalty factor, the constrained variational problem can be transformed into the unconstrained variational problem, as shown in Equation (2).

$$\begin{aligned} \mathcal{L}(\{u_k\}, \{\omega_k\}, \lambda) = & \beta \sum_{k=1}^K \left\| \partial_t \left[\left(\delta(t) + \frac{j}{\pi t} \right) * u_k(t) \right] e^{-j\omega_k t} \right\|_2^2 \\ & + \left\| x_t - \sum_{k=1}^K u_k(t) \right\|_2^2 + \langle \lambda(t), x_t - \sum_{k=1}^K v_k(t) \rangle \end{aligned} \quad (2)$$

where λ and β are the Lagrange multiplication factor and quadratic penalty factor, respectively. The method of solving the optimal solution of $\{v_k\}$, $\{\omega_k\}$, and λ is given in Appendix A.

K is a crucial parameter in VMD. If the value of K is too small, it becomes ineffective in separating different fault components in the arc current $F(t)$. Conversely, if the value of K is too large, it can lead to modal confusion among adjacent modes. Therefore, to achieve optimal decomposition performance, this article sets the value of K to 4.

3. Time–Frequency Composite Recurrence Plots

3.1. Traditional Recurrence Plots

RPs can encode one-dimensional signals into a two-dimensional matrix, effectively capturing the dynamical characteristics of phase space trajectories. The phase space representation of an arc current signal $F(t)$ is depicted in Equation (3).

$$F = \begin{bmatrix} f_1 = (x_1, x_{1+\tau}, \dots, x_{1+(m-1)\tau}) \\ f_2 = (x_2, x_{2+\tau}, \dots, x_{2+(m-1)\tau}) \\ \vdots \\ f_N = (x_{n-(m-1)\tau}, x_{n-(m-2)\tau}, \dots, x_n) \end{bmatrix} \quad (3)$$

where the embedding dimension and time delay are m and τ , respectively. $N = n - (m - 1)\tau$ is the number of phase states in $F(t)$. For example, f_2 is a row vector with m elements and is the second phase states in $F(t)$.

The RP of $F(t)$ can be expressed as

$$RP_{i,j} = \mathcal{H}(\theta - \|f_i - f_j\|) = \begin{cases} 1, & \|f_i - f_j\| > \theta \\ 0, & \|f_i - f_j\| \leq \theta \end{cases} \quad (4)$$

where $i, j = 1, 2, \dots, n - (m - 1)\tau$. $\|f_i - f_j\|$ represents calculating the Euclidean distance between f_i and f_j . $\mathcal{H}(\cdot)$ is heaviside function. θ is the threshold value of Euclidean distance. When two states (f_i and f_j) in the phase space are close to each other, $RP_{i,j}^{m,\tau}$ is set to 1; otherwise, $RP_{i,j}^{m,\tau}$ is set to 0.

3.2. The Basic Principle of Time-Frequency Composite Recurrence Plots

Traditional RPs and their improved forms have the two following shortcomings: ① they solely rely on Euclidean distance, which is not comprehensive enough to measure the similarity between different states in the phase space; ② RPs can only analyze the similarity of different states in the phase space from a time domain perspective, overlooking the fault information implicitly contained in the frequency domain.

To address the above issues, this article proposes a novel TFCRP. The advancement of this method is reflected in two aspects as follows:

- ① By integrating Euclidean distance and cosine distance, a composite similarity index is obtained, overcoming the limitation of the Euclidean norm in analyzing the direction similarity between different states in the phase space;
- ② The arc current signal is decomposed into multiple modes through VMD, and the TFCRP can analyze the composite distance between different phase points in each mode, thereby obtaining time composite recurrence plots (TCRPs). At the same time, the TFCRP can analyze the composite similarity of frequency domain energy states at different instants of time, thereby obtaining frequency composite recurrence plots (FCRPs).

3.2.1. Time Composite Recurrence Plots

Based on VMD, the arc current signal $F(t)$ can be decomposed into multiple modes. The k -th mode is $v_k(t) = \{s_t^k | t = 1, 2, \dots, n\}$ and s_t^k is the t -th point of $v_k(t)$. With the embedding dimension m and the time delay τ , the phase space representation of $v_k(t)$ can be calculated by Equation (5).

$$VT_k = \begin{bmatrix} vt_{k,1} = (s_1^k, s_{1+\tau}^k, \dots, s_{1+(m-1)\tau}^k) \\ vt_{k,2} = (s_2^k, s_{2+\tau}^k, \dots, s_{2+(m-1)\tau}^k) \\ \vdots \\ vt_{k,N} = (s_{n-(m-1)\tau}^k, s_{n-(m-2)\tau}^k, \dots, s_n^k) \end{bmatrix} \quad (5)$$

where $N = n - (m - 1)\tau$ is the number of states in the phase space. For example, $vt_{k,2}$ is a row vector with m elements and is the second state of $v_k(t)$.

The TCRPk of $v_k(t)$ can be expressed as

$$TCRP_{i,j}^k = \beta \|vt_{k,i} - vt_{k,j}\| + (1 - \beta) \text{Cosd}(vt_{k,i}, vt_{k,j}) \quad (6)$$

$$\text{Cosd}(vt_{k,i}, vt_{k,j}) = 1 - \frac{\langle vt_{k,i}, vt_{k,j} \rangle}{\|vt_{k,i}\| \cdot \|vt_{k,j}\|} \quad (7)$$

where $TCRP_{i,j}^k$ an element in the i -th row and j -th column of TCRPk. $\|vt_{k,i} - vt_{k,j}\|$ is the Euclidean distance between $vt_{k,i}$ and $vt_{k,j}$. β denotes the weight factor. $\text{Cosd}(vt_{k,i}, vt_{k,j})$ represents the cosine distance between $vt_{k,i}$ and $vt_{k,j}$, $\text{Cosd} \in [0, 2]$. The smaller the value of Cosd , the higher the directional similarity of the two vectors. $\langle vt_{k,i}, vt_{k,j} \rangle$ is the inner product of $vt_{k,i}$ and $vt_{k,j}$. $\|vt_{k,i}\|$ and $\|vt_{k,j}\|$ are the modular values of $v_{k,i}$ and $v_{k,j}$. β can control the proportion of Euclidean distance and cosine distance; thus, the fusion of these two similarity indexes in the TCRP is realized.

The TCRP can measure the similarity between states in the phase space of modes, from which the mutual interference between different level components is avoided.

3.2.2. Frequency Composite Recurrence Plots

Based on K modes $\{v_k\}$, the time–frequency matrix corresponding to the arc current signal $F(t)$ can be expressed as

$$VF = \begin{bmatrix} v_1 \\ v_2 \\ \vdots \\ v_K \end{bmatrix} = \begin{bmatrix} s_1^1 s_2^1 \cdots s_n^1 \\ s_1^2 s_2^2 \cdots s_n^2 \\ \vdots \\ s_1^K s_2^K \cdots s_n^K \end{bmatrix} = [vf_1 vf_2 \cdots vf_n] \quad (8)$$

where the k -th mode is $v_k(t) = \{s_t^k | t = 1, 2, \dots, n\}$ and s_t^k is the t -th point of $v_k(t)$. VF consists of n column vectors. For example, in VF, the second column vector $vf_2 = [s_2^1; s_2^2; \cdots; s_2^K]$.

The FCRP of $F(t)$ can be calculated by Equation (9).

$$\text{FCRP}_{i,j} = \beta \|vf_i - vf_j\| + (1 - \beta) \text{Cosd}(vf_i, vf_j) \quad (9)$$

$$\text{Cosd}(vf_i, vf_j) = 1 - \frac{\langle vf_i, vf_j \rangle}{\|vf_i\| \cdot \|vf_j\|} \quad (10)$$

where $\text{FCRP}_{i,j}$ is an element in the i -th row and j -th column of the FCRP. $\|vf_i - vf_j\|$ is the Euclidean distance between vf_i and vf_j . β denotes the weight factor. $\text{Cosd}(vf_i, vf_j)$ represents the cosine distance between vf_i and vf_j , $\text{Cosd} \in [0, 2]$. The smaller the value of Cosd , the higher the directional similarity of the two vectors. $\langle vf_i, vf_j \rangle$ is the inner product of vf_i and vf_j . $\|vf_i\|$ and $\|vf_j\|$ are the modular values of vf_i and vf_j . β can control the proportion of Euclidean distance and cosine distance in the FCRP.

In VF, each column vector represents the frequency domain energy distribution of the arc current signal $F(t)$ at different instants of time. By calculating the FCRP, the composite similarity of the frequency domain energy distribution characteristics at different time instants can be analyzed.

3.2.3. Parameter Selection

The weight factor β , decomposition level K , embedding dimension m , and time delay τ are the pivotal parameters for calculating the TFCRP of arc current $F(t)$. The selection of these four parameters has a significant impact on the accuracy of SAF detection. As mentioned in the last paragraph of Section 2, the value of K is set to four in this paper to enable VMD to achieve optimal decomposition performance. The study of [3] analyzed the arc current signal of photovoltaic systems using the mutual information method and the averaged false neighbors method, indicating that the optimal values for the embedding dimension m and time delay τ in the phase space of the arc current are four and two. Therefore, in this article, the embedding dimension m and time delay τ are set to four and two, respectively. In Section 7, the appropriate value of β will be selected by analyzing its influence on SAF detection accuracy.

Figure 2 shows the TCRPs and FCRP obtained based on the TFCRP under a SAF condition and normal condition. The images obtained under normal conditions visually differ significantly from those obtained under the SAF condition, initially demonstrating that the proposed TFCRP can effectively describe the differences in current signals between normal conditions and SAF conditions. In Section 7 of this paper, the performance of the proposed TFCRP will be adequately verified through experimental analysis.

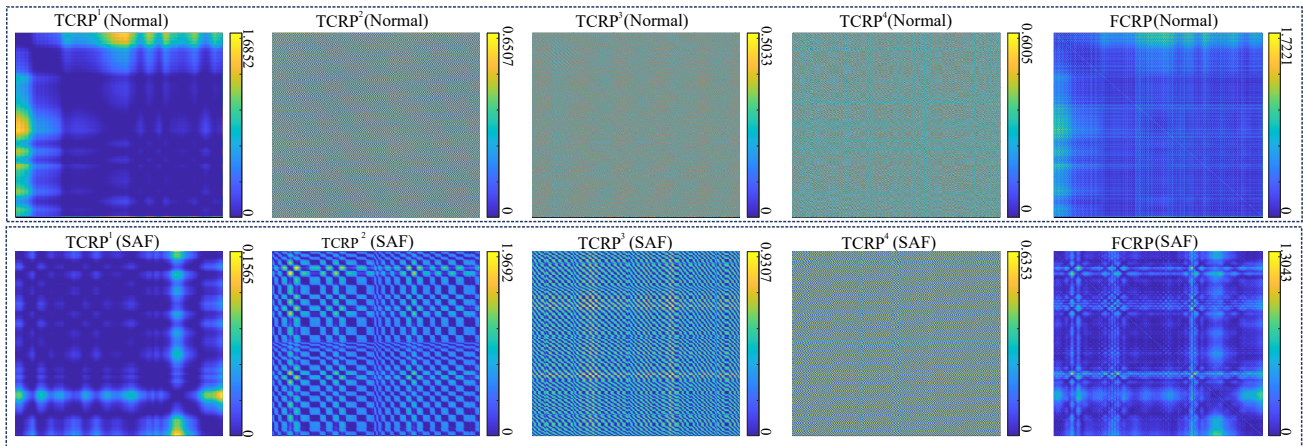


Figure 2. TCRPs and FCRP obtained based on TFCRP under SAF condition and normal condition.

4. Fault Feature Extraction

The size of TCRPs and the FCRP obtained based on the TFCRP is $(n - 6) \times (n - 6)$ and $n \times n$, respectively. n denotes the point number of arc current $F(t)$. For SAF detection, TCRPs and FCRPs should be reduced to extract critical fault information. This paper presents a method for extracting arc fault features based on fractional recurrence entropy and singular value decomposition.

4.1. Fractal Recurrence Entropy

Recurrence entropy (RE) is a key indicator used to measure the dynamic characteristics of a system. RE can be used to calculate the amount of information contained in a recurrence graph, and the smaller the RE, the lower the complexity of the system [23]. SAF introduces complex fluctuation patterns in the current signal; therefore, RE is suitable for distinguishing between normal states and arc fault states as a fault characteristic. However, the traditional method of calculating RE only considers a single fractional order. Fractional calculus is capable of introducing distinctive traits to fractional entropy while preserving the fundamental attributes of Shannon entropy. When extending RE to the fractional derivative form, fractional recurrence entropy (FRE) can be expressed as follows:

$$FRE_{\alpha} = -\sum_{j=2}^N \frac{[p(j)]^{-\alpha}}{\Gamma(\alpha + 1)} \{ \ln [p(j)] + \varphi(1) - \varphi(1 - \alpha) \} p(j) \quad (11)$$

where the digamma function is represented by $\varphi(\cdot)$ and the gamma function is represented by $\Gamma(\cdot)$. The fractional order factor α lies within the range of $(-1, 1)$. When α equals 0, $\Gamma(1)$ is equal to one and FRE becomes the classical RE. In the process of calculating FRE_{α} , in order to binarize, this paper sets the critical level μ to 0.4. The impact of critical level μ on the accuracy of SAF detection will be discussed in Section 7.2. The probability density $p(j)$ represents the distribution of diagonal lines of length j .

FRE can be considered as a generalized form of RE. The FRE obtained for diverse values of α contributes variably to the results of SAF detection [24]. Through the introduction of fractional calculus into RE, the diversity of fault information and the anti-noise capability can be enhanced [25]. In practical applications, α should assume discrete values at specific intervals within the range of $(-1, 1)$. If the interval of α is overly large, the operation time will rise, which is detrimental to real-time SAF detection. By referring to reference [24] and taking into account both the operation time and the fault information diversity, α is allocated at intervals of 0.1 within the range of $[-0.9, 0.9]$. For one sample of the arc current,

four TCRPs and one FCRP can be obtained; therefore, 95 FREs can be extracted from each SAF detection.

4.2. Singular Value Decomposition

SVD is a powerful tool for feature extraction and has been applied in various fields such as battery capacity estimation [26], recommender systems [27], and fault detection [19]. In this paper, SVD is employed to extract abstract features from TCRPs and FCRPs.

Supposing the size of matrix Z is $p \times q$ and $p \geq q$, then the SVD of Z can be defined as follows:

$$Z = VDU^T \quad (12)$$

where the sizes of V and U are $p \times p$ and $q \times q$, respectively. The elements in the main diagonal of $D = \text{diag}(\xi_1, \xi_2, \dots, \xi_q)$ are singular values and $\xi_1 \geq \xi_2 \geq \dots \geq \xi_q$.

Typically, the crucial fault information is mainly contained in the larger singular values with lower order, while the higher-order singular values with smaller values do not contribute significantly to the detection results. By extracting only the first h singular values from TCRPs and the FCRP, we can not only avoid the negative impact of smaller singular values on the detection results but also reduce the computational complexity of SVD, thereby improving the SAF detection speed. In the experimental section, this article will discuss the impact of the number of singular values h on the accuracy and speed of SAF detection in detail, and the value of h will be determined.

5. Extra Tree-Based Classifier

Ensemble algorithms utilize multiple independent base learners to obtain prediction results, providing better generalization capabilities and noise immunity compared to algorithms based on a single classifier. ET is an ensemble algorithm that consists of multiple decision trees. During the training process of ET, the optimal node division is selected from random split values of each feature, effectively reducing the correlation between different trees. ET has been applied to stealthy cyber-attack detection [28], object detection [29], and endomicroscopic image classification [30].

This paper employs ET as the classifier to explore the complex nonlinear relationship between the extracted feature vectors based on singular values and the fault states. When using ET to handle classification problems, it is necessary to use all samples to train each tree in ET. The diagram of ET is shown in Figure 3. In Figure 3, ET contains C decision trees, each of which is trained based on a complete dataset. After training all decision trees, the training of ET is completed. The trained C decision trees constitute the trained ET, which can handle unknown samples. When a sample is input to the trained ET, each decision tree in the ET will independently output the corresponding prediction result. For classification problems, the output of ET is obtained based on the principle of majority voting.

The training process of the trees primarily involves implementing a random feature value splitting at each node, with the following splitting steps [30]:

- (1) m features $\{sv_1, sv_2, \dots, sv_m\}$ are randomly selected.
- (2) Calculating the maximum value sv_i^{max} and minimum value sv_i^{min} of the feature sv_i in the dataset.
- (3) The splitting point sv_i^f of feature sv_i is randomly selected in $[sv_i^{min}, sv_i^{max}]$.
- (4) Calculating the Gini index G_i^f of the feature sv_i with the splitting point sv_i^f .
- (5) Selecting the splitting point with the maximum Gini index as the final splitting point for feature sv_i to achieve the partitioning of the current node.

Each node in the tree is split according to the aforementioned process, enabling the training of all trees in ET. During the training process, 5-fold cross-validation is used to

verify the performance of ET with different numbers of trees. In this paper, the applicable number of trees in ET is set to 30.

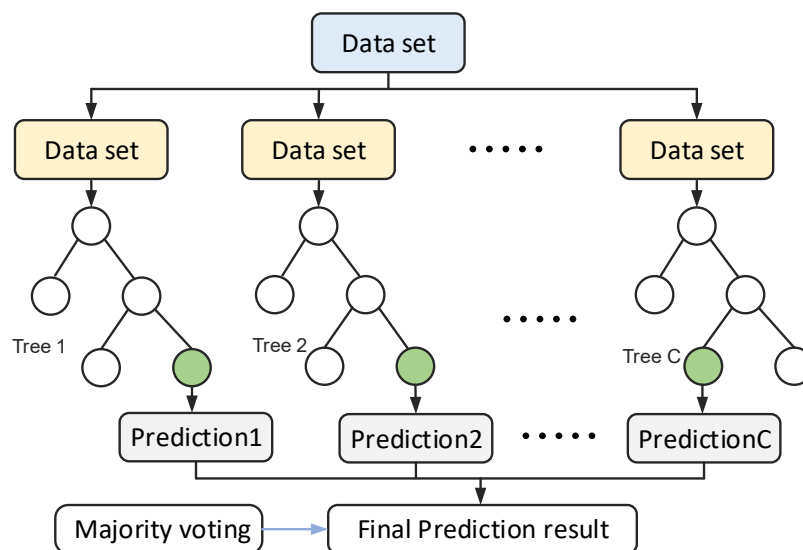


Figure 3. The diagram of ET.

6. Experimental Data Collection

To validate the performance of the proposed SAF detection method, an experimental platform is established, as shown in Figure 4. The platform can simulate SAFs under different load types of photovoltaic systems, and arc current data under different conditions can be obtained and analyzed through a data acquisition and analysis system. In Figure 4, the PV simulated source can supply power to three types of loads, namely the inverter (YanXu YXMG-SGA05), DC-DC converter, and resistor. The output voltage range of the PV simulated source is 50 V to 400 V. The selector switch allows for the selection of the load type in the circuit. The electronic arc generator is connected in series to the circuit. Under normal conditions, the two electrodes of the arc generator are closed. The arc fault generator controller then separates the two electrodes at a certain speed, generating an SAF. According to standard UL1699B, the separation speed and arc length are set to 5 mm/s and 1.1 mm, respectively. The current signals collected by the current sensor are transmitted to the microprogrammed control unit (MCU) for storage through a data acquisition (DAQ) board, and the PC can access the MCU and download the saved data. The algorithm programming in this article is implemented using Python 3.7, with a programming environment of Windows 11 operating system, Intel-Core-i5 CPU, and 32 GB RAM. The MCU is equipped with a Cortex-A72 CPU and 4 GB RAM.

Figure 5 illustrates the system current waveforms across various load types and operating conditions. Under SAF conditions, the current signal exhibits more pronounced random fluctuations compared to the steady-state current signal observed under normal conditions. However, under normal conditions, transient system actions (such as voltage fluctuations and MTTP operations) can introduce arc-like noise into the current signal. Additionally, visually, the current fluctuation state caused by the high-frequency switching action of the inverter is similar to the fluctuation state of the arc current of a resistor load. Therefore, the diverse operating states and load types in PV systems pose significant challenges for SAF detection.

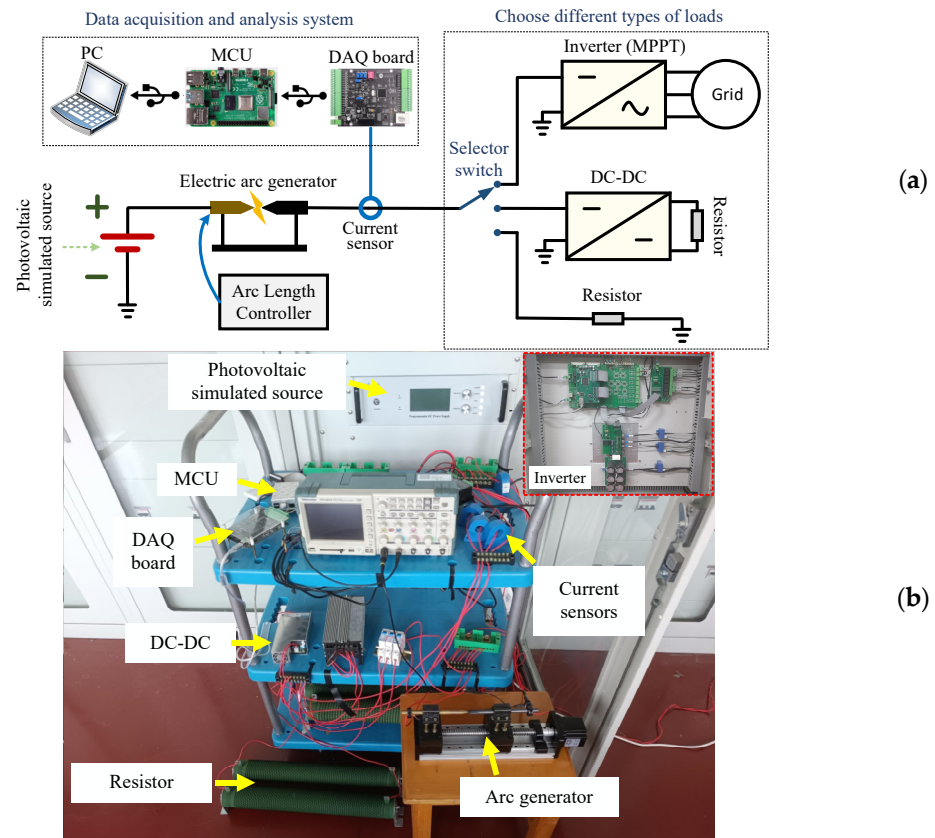


Figure 4. The experimental platform: (a) diagram; (b) actual platform.

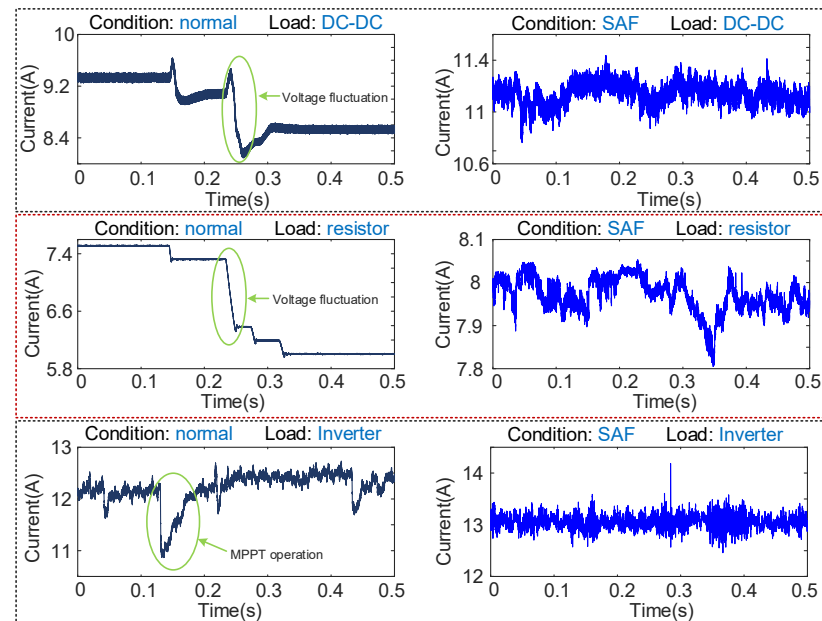


Figure 5. Current waveforms under different load types and different operating conditions.

Although the arc current exhibits differences under different operating conditions, arc faults consistently alter the time domain fluctuations and spectral energy distribution of the current signal. Before and after arc faults, subtle changes occur in the similarity of the high-dimensional time–frequency space of the current signal. Thus, the TFCRP aims to simultaneously extract this critical consistency similarity information from both the time and frequency domains, which is beneficial for the classifier to accurately distinguish between normal conditions and arc faults.

Based on the established experimental platform, a total of 31,500 samples were collected. Table 1 presents the operating conditions corresponding to the dataset. In each case, 60% of the samples was used to constitute the training dataset, while the remaining 40% was used for the test dataset. Consequently, the training dataset contains 18,900 samples, and the test dataset contains 12,600 samples. The characteristics of arc faults can be effectively captured with a sampling rate of 100 kHz [3]; hence, the sampling rate of the DAQ board was set to 100 kHz in this study, with each sample containing 512 data points. To verify the adaptability of the proposed method, the samples under normal conditions included transient system actions.

Table 1. Experimental conditions corresponding to the dataset.

State	Voltage(V)	Current(A)	Label	Number of Samples	Load Type
Normal condition	50~400	2~17	1	2500	Resistor
				2500	DC-DC
				5800	Inverter
SAF condition			2	2200	Resistor
				2200	DC-DC
				5800	Inverter

7. Analysis of Experimental Results

7.1. Experimental Results of Proposed Method

This article validates the performance of the proposed method based on the dataset constructed in Section 6. Table 2 presents the detection results of the proposed method under different conditions. The proposed method achieves an overall detection accuracy of 98.75%, with only 158 samples out of 12,600 samples in the test set being misdetected.

Table 2. Detection results of the proposed method under different conditions.

	Detection Results	Load Type
Normal condition	98.80% (1482/1500)	DC-DC
	99.53% (1493/1500)	Resistor
	99.19% (3452/3480)	Inverter
SAF condition	97.95% (1293/1320)	DC-DC
	99.09% (1308/1320)	Resistor
	98.10% (3414/3480)	Inverter
Overall detection accuracy: 98.75% (12,442/12,600)		

The detection accuracy under normal conditions is 99.18% (6427/6480), and the detection accuracy corresponding to the resistor load (99.53%) is higher than that of DC-DC (98.80%) and inverter (99.19%) loads. This is attributed to the fact that the DC-DC and inverter are nonlinear loads, and the arc-like noise introduced by their internal high-frequency switching action enhances the difficulty of detection.

Under SAF conditions, the detection accuracy is 98.28% (6015/6120), which is significantly lower than that under normal conditions. SAF is an unstable plasma state, and compared to normal conditions, the random fluctuations of the arc current can cause stronger interference to the detection algorithm, resulting in a significantly lower detection accuracy under SAF conditions. When the load types are DC-DC converter and inverter, the detection accuracies under the SAF condition are 97.95% and 98.10%, respectively. Under the SAF condition, the detection accuracy of the resistor is 99.09%. This indicates that the

high-frequency switching state and energy control mechanism of nonlinear loads (DC-DC converter and inverter) introduce more complex fluctuation patterns in the arc current signal, making it more challenging to accurately identify arc faults under nonlinear loads compared to linear loads.

The experimental results demonstrate that the proposed method can handle false alarms under normal conditions and can detect arc faults in multiple operating states of the system with an accuracy of over 98.5%, thus indicating the effectiveness of the proposed method.

7.2. Impact of Typical Factors on Detection Performance

Based on the analysis in Sections 2 and 3, it is evident that the weight factor β (in TFCRP), the number of singular values h signal, critical level μ , and the decomposition method have significant impacts on the detection performance. This section explores the influence of these three factors on the detection performance.

Figure 6 shows the detection accuracy under different values of β . If $\beta = 0$, it is indicated that the TFCRP only uses cosine distance to measure the similarity between different states in the phase space, with a detection accuracy of 97.93%. If $\beta = 1$, it is indicated that TFCRP only uses Euclidean distance to measure the similarity between different states in the phase space, with a detection accuracy of 98.55%. The maximum detection accuracy of 98.76% is achieved when $\beta = 0.7$. The results in Figure 6 show that the employing of a composite similarity index has a beneficial effect on improving detection accuracy.

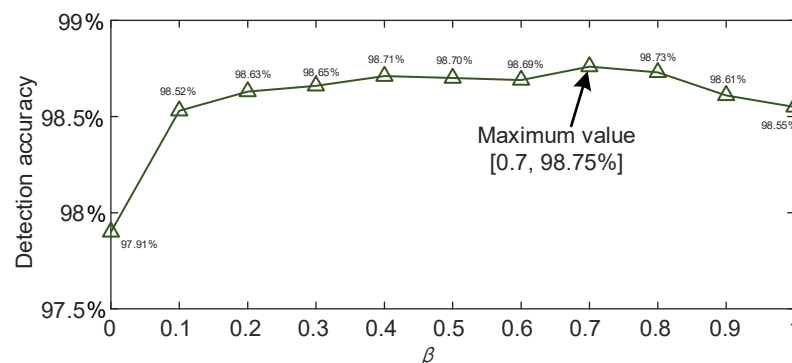


Figure 6. The detection accuracy under different values of β .

Figure 7 displays the relationship between detection accuracy and detection time for varying numbers of singular values. As the number of singular values (h) increases, the detection accuracy initially rises sharply before stabilizing. Specifically, when h equals 13, the detection accuracy peaks at 98.75%. Beyond this point, further increases in h do not enhance detection accuracy but linearly prolong the detection time. This suggests that once a certain threshold of singular values is reached, additional extraction singular values introduce redundant information that fails to meaningfully improve performance while increasing computational overhead. Thus, for a balance of accuracy and efficiency, this paper sets h to 13. Figure 8 presents the corresponding detection accuracy for various critical level μ values. The critical level μ is capable of achieving binary of recurrence plots. If the μ value is overly large, only distant points in the recurrence plots can contain information, resulting in significant information loss. If the μ value is too small, there will be redundant fault information. The maximum detection accuracy is attained at $\mu = 0.4$, and therefore, this paper sets μ to 0.4. For feature visualization, the t-distributed stochastic neighbor embedding (t-SNE) method is employed to reduce the dimensionality of the 170-dimensional fault features to two dimensions. As depicted in Figure 9, the t-SNE

visualization of the extracted singular values reveals a clear separation between most data points under normal conditions and SAF conditions, with only a minority exhibiting overlap. This underscores the effectiveness of the feature vector constructed from the extracted singular values.

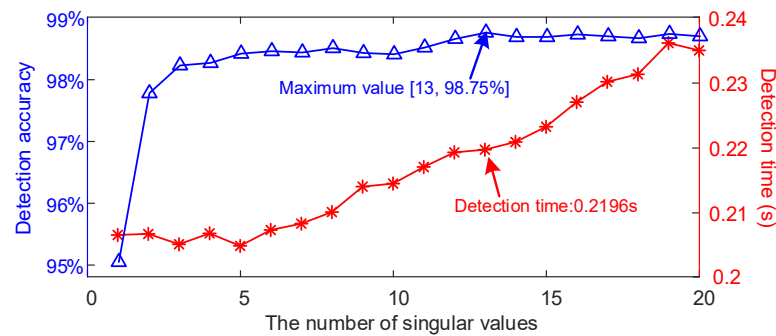


Figure 7. Detection accuracy and detection time corresponding to different numbers of singular values.

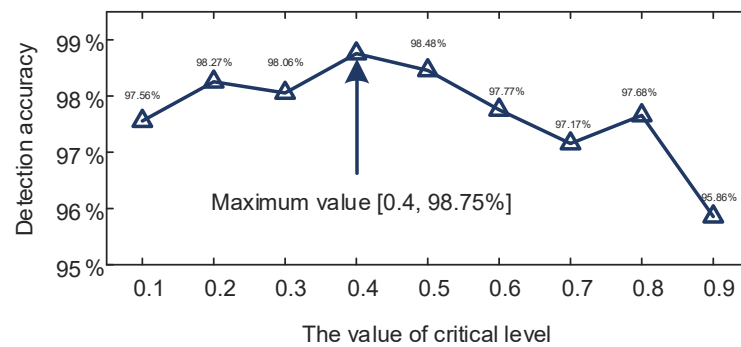


Figure 8. The detection accuracy under different values of critical levels.

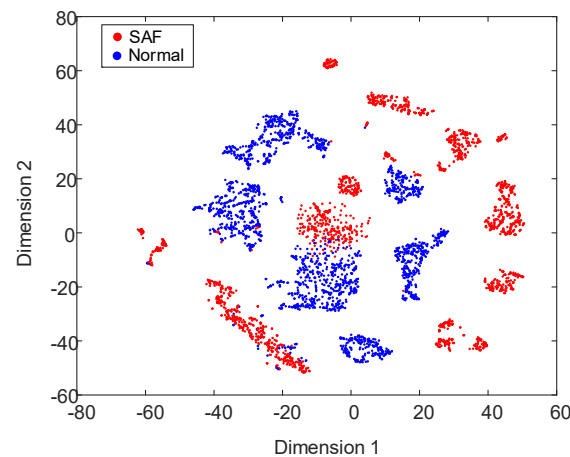


Figure 9. The t-SNE visualization of extracted singular values under normal conditions and SAF conditions.

Figure 10 shows the detection accuracy under different signal decomposition methods. Wavelet transform (WT) is based on the bior3.1 wavelet basis function [31], and both WT and EMD decompose the current signal into four components. The detection accuracy of WT and empirical mode decomposition are 91.59% and 95.62%, respectively. The experimental results show that in this paper, compared with WT and EMD, VMD is more suitable for combining with TFCRPs to form an SAF detection algorithm. Therefore, VMD is chosen to implement the decomposition of the arc current signal.

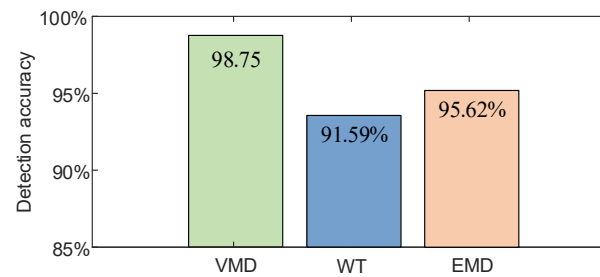


Figure 10. The detection accuracy under different signal decomposition methods.

The voltage levels and load characteristics in aviation DC power supply systems, electric vehicle DC power supply systems, and shipboard DC systems differ significantly from those in photovoltaic systems, which poses challenges for the application of the method proposed in this paper in these systems. To adapt the arc fault detection algorithm proposed in this paper for application in these systems, the following adjustments should be considered: (1) select an appropriate signal decomposition algorithm tailored to the specific characteristics of each system and (2) carefully determine the values of the three key parameters, namely the weight factor β , the number of singular values h , and the critical level μ , ensuring they are optimized for the target system.

7.3. Comparing the Performance of Different Methods

In this article, the proposed method (PR1) is compared with eight existing methods to further validate the reliability of PR1.

Comparison method CO1: CO1 is a method based on an autocorrelation algorithm (AAL) [6]. The Pearson correlation coefficient value of the current signal is extracted using ALL. If the Pearson correlation coefficient value exceeds the set threshold, it indicates SAF occurred in the system; otherwise, the system is in a normal state. In CO1, the time interval is 40 ms and the optimal threshold 0.3842 can be calculated based on the C4.5 algorithm.

Comparison method CO2: CO2 is a method based on RF [32]. The random fluctuations of the current signal are measured by extracting the average (AVE), median (MED), variance (VAR), root mean square (RMS), and the difference between the maximum and minimum values (DMM) from the current signal, and the extracted features are input into RF to obtain the detection results. In CO2, the number of trees in RF is set to 30.

Comparison method CO3: CO3 is a method based on a back propagation neural network (BPNN) [19]. Firstly, the current signal is converted into a two-dimensional matrix based on the improved recurrence plots (IRPs). Then, singular values, DET, LDL, TND, and LAM are extracted from the matrix to construct a feature vector. Finally, the BPNN is used to process the feature vector and obtain the detection results. The structure of the BPNN is [9 20 2]. The embedding dimension m and time delay τ of IRP are four and two, respectively.

Comparison method CO4: CO4 is a method based on SVMs [33]. The arc current is decomposed into eight modes using VMD, and then the sample entropy (SE) and energy entropy of the first three modes are extracted to construct a feature vector. An SVM is used to process the feature vector to achieve arc fault detection. In the SVM, the penalty parameter c and kernel parameter g are optimized using the particle swarm optimization algorithm. The relative tolerant r and embedding dimension m are set to 2 and 0.1, respectively.

Comparison method CO5: CO5 is a method based on a gradient boosted decision tree (GBDT) [34]. The variance, normalized energy ratio, and energy entropy of the current signal are extracted based on the db2 wavelet, and then the energy entropy of the current signal is extracted based on empirical mode decomposition. GBDT is used to fuse the

extracted multiple features and obtain the detection results. The number of wavelet layers is five and the number of trees in the GBDT is 30.

Comparison method CO6: CO6 is a method based on VGG11 [35]. VGG11 is a deep learning model that constructs a deep network by stacking multiple smaller convolutional layers and pooling layers to enhance the feature extraction capability. VGG11 consists of 11 convolutional layers and three fully connected layers. For details about VGG11, please refer to the literature [35]. During the training process, the learning rate of VGG11 is set to 0.0007 and the number of training epochs is set to 500.

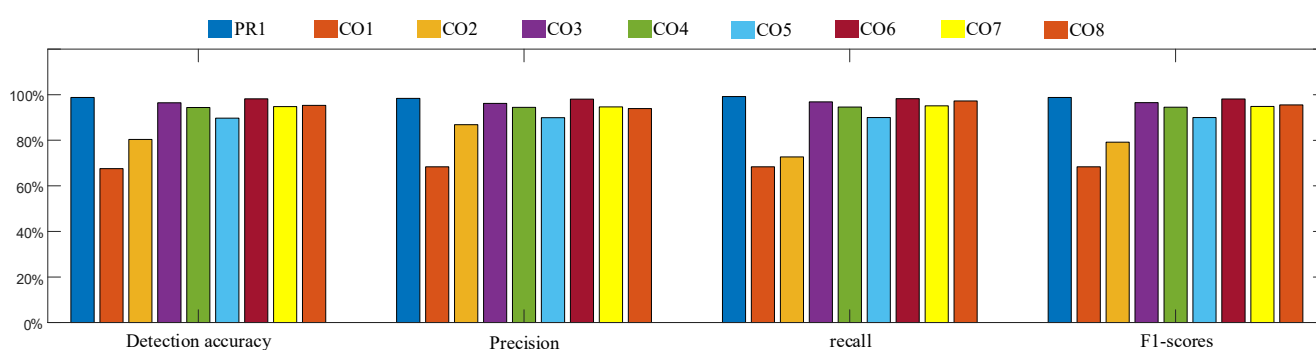
Comparison method CO7: CO7 is a method based on LOCALVIT [36]. LOCALVIT introduces a locality mechanism in the transformer's feedforward network. This mechanism can effectively combine the locality of a convolutional neural network (CNN) with the global connectivity of the visual transformer and can improve the performance of networks without increasing the complexity of the model. For details about VGG11, please refer to reference [36]. In this paper, the learning rate for the training of VGG11 is set to 1×10^{-5} and the number of training epochs is 500.

Comparison method CO8: CO8 is a method based on weighted multi-scale fractional permutation entropy (WMFPE) [37]. Firstly, the multi-scale fractional permutation entropy is extracted from the current signal. Then, the optimal weights of different permutation entropy values are obtained based on particle swarm optimization, and the features are input into an SVM to obtain the detection results. By referring to [37], coarse-grain scale, fractional-order factor α , embedding dimension m , and time lag τ are set as 20, 0.5, 4, and 1, respectively.

Table 3 and Figure 11 show the detection results of different methods. Some useful metrological field parameters like detection accuracy, precision, recall, and the F1 score are presented. The detection accuracy of PR1 (98.75%) is higher than that of the comparative methods CO1 (67.52%), CO2 (80.33%), CO3 (96.42%), CO4 (94.37%), CO5 (89.69%), CO6 (98.16%), CO7 (94.81%), and CO8 (95.34%). CO1 solely detects SAF based on the threshold of correlation features extracted using ALL, from which it is hard to effectively adapt to the different operating conditions of PV systems. CO2, CO3, CO4, CO5, and CO8 can fuse different types of features based on machine learning algorithms. CO2, CO3, CO4, CO5, and CO8 are able to improve the detection accuracy compared to CO1. CO6 and CO7 adaptively mine abstract fault information in arc current signals based on VGG11 and LOCALVIT, respectively. The detection accuracy of CO6 and CO7 is 98.16% and 94.81%, which are still lower than the detection accuracy of PR1. The detection accuracy of CO3, CO4, CO6, CO7, and CO8 is close to that of the proposed method. However, when the detection accuracy exceeds 95%, increasing it by 0.5% is a challenging task [32,38]. SAFs in photovoltaic systems can generate temperatures as high as 3000 °C, which can easily lead to fire accidents. Therefore, even if the detection accuracy is increased by 0.59%, it has a positive significance for maintaining the safety of photovoltaic systems. As shown in Table 3, precision, recall, and the F1 score of the proposed method are higher than the compared methods; it is indicated that the proposed method has more advantages to prevent false alarms and ensure that fault samples are correctly identified. Comparing with other eight methods, PR1 can more effectively distinguish between SAF conditions and normal conditions by mining composite correlation information in the time–frequency domain of arc current signals in high-dimensional phase space.

Table 3. The performance of different detection methods.

	Feature Extraction Method	Classifier	Training Time	Test Time	Detection Accuracy	Precision	Recall	F1 Scores
PR1	VMD+TFCRP+FRE+SVD	ET	0.55 s	209 ms	98.75%	98.39%	99.18%	98.78%
CO1 [6]	AAL	Threshold	0.12 s	0.07 ms	67.52%	68.34%	68.35%	68.34%
CO2 [32]	AVE+MED+VAR+RMS+DMM	RF	0.61 s	0.05 ms	80.33%	86.84%	72.68%	79.13%
CO3 [19]	IRP+RQA+SVD	BPNN	42 s	16.8 ms	96.42%	96.18%	96.86%	96.52%
CO4 [33]	VMD+SE+EE	SVM	2.38 s	141 ms	94.37%	94.46%	94.56%	94.51%
CO5 [34]	WT+EMD	GBDT	4.93 s	3.5 ms	89.69%	89.92%	89.98%	89.95%
CO6 [35]	\	VGG11	7571 s	5.9 ms	98.16%	98.04%	98.25%	98.14%
CO7 [36]	\	LOCALVIT	6750 s	4.6 ms	94.81%	94.64%	95.09%	94.86%
CO8 [37]	WMFPE	SVM	2.79 s	21.96 ms	95.34%	93.88%	97.26%	95.54%

**Figure 11.** The visualization bar chart of the detection results of different methods.

The training time of PR1 (0.55 s) is slightly higher than that of CO1 (0.12 s) and is lower than that of CO2, CO3, CO4, CO5, and CO8. The complexity of the threshold calculation process in CO1 is significantly lower than the machine learning training processes of the other eight methods. In PR1, the ET with random splitting of nodes can acquire a lower training time compared to machine learning algorithms such as RF, the SVM, and GBDT. The feature vector dimension corresponding to PR1, CO2, CO4, CO5, and CO8 are 65, 5, 6, 14, and 20, respectively. With the same number of training samples, the feature vector dimension of ET is significantly higher than those of RF, the SVM, and GBDT, and the training time of ET is shorter than that of RF, the SVM, and GBDT. It is proved that ET used in PR1 has a significant advantage in training efficiency. CO3, CO6, and CO7 use the backpropagation algorithm to train BPNN, VGG11, and LOCALVIT, respectively, resulting in the training times of CO3 (42 s), CO6 (7571 s), and CO7 (7571 s) being significantly longer compared to the other six methods. Notably, the training processes of the BPNN, VGG11, and LOCALVIT require the use of an NVIDIA RTX3050 GPU, which improves the hardware costs.

Among the nine evaluated algorithms, PR1 exhibits the longest test time of 209 ms. This is attributed to the intricate process of mining composite similarity information concealed within the time–frequency domain of arc current signals, which imposes substantial computational demands. In contrast, CO1 and CO2 boast test times under 1 ms due to their relatively straightforward feature extraction procedures—correlation feature extraction in CO1 and time-domain feature calculation in CO2. CO3, CO5, and CO8 involve complex feature extraction methods incorporating data decomposition algorithms like SVD, WT, EMD, and multi-scale techniques, resulting in notably longer test times compared to CO1 and CO2, albeit still less than one-tenth of PR1’s duration. In CO4, the iterative optimization process involved in decomposing arc current using VMD, coupled with the

computation of distances between distinct phase states for SE extraction, contributes to a test time exceeding 140 ms.

Despite PR1's relatively longer test time, it emerges as the superior algorithm in terms of detection accuracy, underscoring its reliability and advancement. The ET classifier employed in PR1 excels in training efficiency. While PR1's 209 ms test time is higher than that of six other methods, it remains well within the 2.5 s detection threshold stipulated by the UL1699B standard [38,39], rendering its detection speed acceptable and compliant with industry requirements. Consequently, the proposed method in this paper holds considerable promise for practical engineering applications.

8. Conclusions

This article introduces a novel SAF detection method leveraging a TFCRP tailored to adapt to the complex operating conditions of PV systems. Initially, the arc current is decomposed into distinct modes using VMD, effectively mitigating potential mutual interference among various frequency components during subsequent feature extraction processes. Subsequently, a TFCRP is employed to process these modes, transforming the arc current into two-dimensional matrices. This transformation facilitates the extraction of crucial time–frequency composite correlation fault information. Ultimately, the FREs and singular values extracted from these matrices are fed into an ET classifier to yield precise detection results.

The cornerstone contribution of this article lies in the introduction of an innovative TFCRP technique. The TFCRP adeptly integrates Euclidean distance and cosine distance within a composite similarity index, surpassing the limitations of traditional RPs in analyzing directional similarity between various phase space states. Furthermore, by processing the modes derived from VMD, the TFCRP uniquely captures the composite similarity information across frequency energy states at different time instances, where the traditional RP falls short in extracting fault information within the frequency domain.

The performance of the proposed method is substantiated through experimental data encompassing diverse operating conditions. With a detection accuracy of 98.75%, surpassing six comparative methods, the proposed method adeptly identifies SAF occurrences while effectively mitigating false alarms during transient conditions. Moreover, its detection time of 209 ms aligns with UL1699B standards, underscoring its practical potential for engineering applications.

Future endeavors will explore the application of TFCRPs in broader contexts, including mechanical fault diagnosis and power electronic device fault diagnosis. The principle of the SAF detection method proposed in this paper is complex. How to effectively run the proposed method in real time on an embedded processor to ensure the safe and stable operation of actual photovoltaic systems is a very challenging task. If the parallel computing of different steps in the feature extraction process is implemented based on FPGA, the online detection speed can be effectively improved.

Author Contributions: Conceptualization, Z.Y.; Methodology, Z.Y.; Software, Z.Y. and H.O.; Validation, Z.Y.; Formal analysis, Z.Y.; Investigation, Z.Y.; Resources, Z.Y.; Data curation, Z.Y.; Writing—original draft, Z.Y.; Writing—review & editing, Z.Y., H.O., J.L., L.W. and S.Y.; Visualization, Z.Y.; Supervision, L.W. and S.Y.; Project administration, Z.Y.; Funding acquisition, S.Y. All authors have read and agreed to the published version of the manuscript.

Funding: This work was supported by the National Natural Science Foundation of China, 51877102.

Data Availability Statement: The data presented in this study are available on request from the corresponding author, the data are not publicly available due to privacy or ethical restrictions.

Conflicts of Interest: The authors declare no conflicts of interest.

Nomenclature

SAF	Series arc fault
PV	Photovoltaic
TFCRP	Time–frequency composite recurrence plot
VMD	Variational mode decomposition
ET	Extra tree
FRE	Fractional recurrence entropy
EMD	Empirical mode decomposition
SVM	Support vector machine
RF	Random forests
RP	Recurrence plot
SVD	Singular value decomposition
RE	Recurrence entropy
TCRP	Time composite recurrence plot
FCRP	Frequency composite recurrence plot
MCU	Microprogrammed control unit
DAQ	Data acquisition
AAL	Autocorrelation algorithm
AVE	Average
MED	Median
VAR	Variance
RMS	Root mean square
DMM	The difference between the maximum and minimum values
BPNN	Back propagation neural network
t-SNE	t-distributed stochastic neighbor embedding
BPNN	Back propagation neural network
IRP	Improved recurrence plot
SE	Sample entropy
GBDT	Gradient boosted decision tree
CNN	Convolutional neural network
MFPE	Multi-scale fractional permutation entropy

Appendix A

In VMD, the optimal solution of $\{v_k\}$, $\{\omega_k\}$, and λ can be obtained based on the alternate direction method of multipliers, as shown in Equation (A1).

$$\left\{ \begin{array}{l} \hat{u}_k^{n+1}(\omega) = \frac{\hat{S}(\omega) - \sum_{i \neq k} \hat{v}_i(\omega) + \frac{\hat{\lambda}(\omega)}{2}}{1 + 2\zeta(\omega - \omega_k)^2} \\ \hat{\lambda}^{n+1}(\omega) = \hat{\lambda}^{(n)}(\omega) + \zeta \left(\hat{f}(\omega) - \sum_{k=1}^K \hat{v}_k^{n+1}(\omega) \right) \\ \omega_k^{n+1} = \frac{\int_0^\infty \omega |\hat{v}_k^{(n+1)}(\omega)|^2 d\omega}{\int_0^\infty |\hat{v}_k^{(n+1)}(\omega)|^2 d\omega} \end{array} \right. \quad (\text{A1})$$

where after processing sequence $v_k^{n+1}(t)$, $S(t)$ and $\lambda_k^{n+1}(t)$, based on Fourier transform, $\hat{v}_k^{n+1}(\omega)$, $\hat{S}(\omega)$, and $\hat{\lambda}^{n+1}(\omega)$ can be obtained.

Stopping the iteration when the condition is satisfied, as shown in Equation (A2), gives the following:

$$\sum_{k=1}^K \frac{\|\hat{v}_k^{n+1}(\omega) - \hat{v}_k^n(\omega)\|_2^2}{\|\hat{v}_k^n(\omega)\|_2^2} \geq \varepsilon \quad (\text{A2})$$

where ε denotes convergence precision.

References

1. Trifkovic, M.; Sheikhzadeh, M.; Nigim, K.; Daoutidis, P. Modeling and Control of a Renewable Hybrid Energy System with Hydrogen Storage. *IEEE Trans. Control Syst. Technol.* **2014**, *22*, 169–179. [[CrossRef](#)]
2. Yin, Z.; Wang, L.; Yang, S.; Gao, Y. A Series Arc Fault Diagnosis Method in DC Distribution Systems Based on Multiscale Features and Random Forests. *IEEE Sens. J.* **2023**, *23*, 2605–2617. [[CrossRef](#)]
3. Amiri, A.; Samet, H.; Ghanbari, T. Recurrence Plots Based Method for Detecting Series Arc Faults in Photovoltaic Systems. *IEEE Trans. Ind. Electron.* **2022**, *69*, 6308–6315. [[CrossRef](#)]
4. Xiong, Q.; Feng, X.; Gattozzi, A.L.; Liu, X.; Zheng, L.; Zhu, L.; Ji, S.; Hebner, R.E. Series Arc Fault Detection and Localization in DC Distribution System. *IEEE Trans. Instrum. Meas.* **2020**, *69*, 122–134. [[CrossRef](#)]
5. Gu, J.; Lai, D.; Wang, J.; Huang, J.; Yang, M. Design of a DC Series Arc Fault Detector for Photovoltaic System Protection. *IEEE Trans. Ind. Appl.* **2019**, *55*, 2464–2471. [[CrossRef](#)]
6. Miao, W.; Wang, Z.; Wang, F.; Lam, K.; Pong, P. Multicharacteristics Arc Model and Autocorrelation-Algorithm Based Arc Fault Detector for DC Microgrid. *IEEE Trans. Ind. Electron.* **2023**, *70*, 4875–4886. [[CrossRef](#)]
7. Yin, Z.; Wang, L.; Zhang, B.; Meng, L.; Zhang, Y. An Integrated DC Series Arc Fault Detection Method for Different Operating Conditions. *IEEE Trans. Ind. Electron.* **2021**, *68*, 12720–12729. [[CrossRef](#)]
8. Miao, W.; Xu, Q.; Lam, K.; Pong, P.; Poor, H. DC Arc-Fault Detection Based on Empirical Mode Decomposition of Arc Signatures and Support Vector Machine. *IEEE Sens. J.* **2021**, *21*, 7024–7033. [[CrossRef](#)]
9. Jiang, J.; Li, W.; Wen, Z.; Bie, Y.; Schwarz, H.; Zhang, C. Series Arc Fault Detection Based on Random Forest and Deep Neural Network. *IEEE Sens. J.* **2021**, *21*, 17171–17179. [[CrossRef](#)]
10. Cui, R.; Zhang, Z.; Tong, D.; Cui, J. Aviation AC Series Arc Fault Detection Based on Improve Empirical Wavelet Transform Multi-Feature Fusion. *Trans. China Electrotech. Soc.* **2022**, *37*, 3148–3161.
11. Jiang, R.; Wang, Y.; Gao, X.; Bao, G.; Hong, Q.; Booth, C. AC Series Arc Fault Detection Based on RLC Arc Model and Convolutional Neural Network. *IEEE Sens. J.* **2023**, *23*, 14618–14627. [[CrossRef](#)]
12. Song, J.; Wu, X.; Qian, L.; Lv, W.; Wang, X.; Lu, S. PMSLM Eccentricity Fault Diagnosis Based on Deep Feature Fusion of Stray Magnetic Field Signals. *IEEE Trans. Instrum. Meas.* **2024**, *73*, 3506012. [[CrossRef](#)]
13. Bai, Y.; Yang, J.; Wang, J.; Zhao, Y.; Li, Q. Image representation of vibration signals and its application in intelligent compound fault diagnosis in railway vehicle wheelset-axlebox assemblies. *Mech. Syst. Signal Process.* **2021**, *152*, 1–14. [[CrossRef](#)]
14. Cui, R.; Tong, D.; Li, Z. Aviation arc Fault Detection Based on Generalized S Transform. *Proc. CSEE* **2021**, *41*, 8241–8249.
15. Jiang, R.; Bao, G.; Hong, Q.; Booth, C. A Coupling Method for Identifying Arc Faults Based on Short-Observation-Window SVDR. *IEEE Trans. Instrum. Meas.* **2021**, *70*, 3513810. [[CrossRef](#)]
16. Jiang, R.; Zheng, Y. Series Arc Fault Detection Using Regular Signals and Time-Series Reconstruction. *IEEE Trans. Ind. Electron.* **2023**, *70*, 2026–2036. [[CrossRef](#)]
17. Ahmadi, M.; Samet, H.; Ghanbari, T. A New Method for Detecting Series Arc Fault in Photovoltaic Systems Based on the Blind-Source Separation. *IEEE Trans. Ind. Electron.* **2020**, *67*, 5041–5049. [[CrossRef](#)]
18. Gao, H.; Wang, Z.; Tang, A.; Han, C.; Guo, F.; Li, B. Research on Series Arc Fault Detection and Phase Selection Feature Extraction Method. *IEEE Trans. Instrum. Meas.* **2021**, *70*, 2004508. [[CrossRef](#)]
19. Liu, Y.; Lv, Z.; Zhang, S.; Zhang, L.; Guo, F. Feature Extraction and Detection Method of Series Arc Faults in a Motor With Inverter Circuits Under Vibration Conditions. *IEEE Trans. Ind. Electron.* **2024**, *71*, 6294–6303. [[CrossRef](#)]
20. Zhang, Y.; Hou, Y.; Ouyang, K.; Zhou, S. Multi-scale signed recurrence plot based time series classification using inception architectural networks. *Pattern Recognit.* **2022**, *123*, 108385. [[CrossRef](#)]
21. Luo, H.; Bo, L.; Peng, C.; Hou, D. Detection and quantification of oil whirl instability in a rotor-journal bearing system using a novel dynamic recurrence index. *Nonlinear Dyn.* **2023**, *111*, 2229–2261. [[CrossRef](#)]
22. Wang, L.; Qiu, H.; Yang, P.; Mu, L. Arc fault detection algorithm based on variational mode decomposition and improved multi-scale fuzzy entropy. *Energies* **2021**, *14*, 4137. [[CrossRef](#)]
23. Marwan, N.; Romano, M.; Thiel, M.; Kurths, J. Recurrence plots for the analysis of complex systems. *Phys. Rep.* **2007**, *438*, 237–329. [[CrossRef](#)]
24. Sun, Y.; Cao, Y.; Xie, G.; Wen, T. Sound based fault diagnosis for RPMs based on multi-scale fractional permutation entropy and two-scale algorithm. *IEEE Trans. Veh. Technol.* **2021**, *70*, 11184–11192. [[CrossRef](#)]
25. Zhang, B.; Shang, P. Cumulative Permuted Fractional Entropy and its Applications. *IEEE Trans. Neural Netw. Learn. Syst.* **2021**, *32*, 4946–4955. [[CrossRef](#)] [[PubMed](#)]
26. Zhou, N.; Zhao, X.; Han, B.; Li, P.; Wang, Z.; Fan, J. A novel quick and robust capacity estimation method for Li-ion battery cell combining information energy and singular value decomposition. *J. Energy Storage* **2022**, *50*, 1–12. [[CrossRef](#)]
27. Movafegh, Z.; Rezapour, A. Improving collaborative recommender system using hybrid clustering and optimized singular value decomposition. *Eng. Appl. Artif. Intell.* **2023**, *126*, 1–17. [[CrossRef](#)]

28. Camana, M.; Ahmed, S.; Garcia, C.; Koo, I. Extremely Randomized Trees-Based Scheme for Stealthy Cyber-Attack Detection in Smart Grid Networks. *IEEE Access* **2020**, *8*, 19921–19933. [[CrossRef](#)]
29. Sonny, A.; Kumar, A.; Cenkeramaddi, L. Carry Object Detection Utilizing mmWave Radar Sensors and Ensemble-Based Extra Tree Classifiers on the Edge Computing Systems. *IEEE Sens. J.* **2023**, *23*, 20137–20149. [[CrossRef](#)]
30. Desir, C.; Petitjean, C.; Heutte, L.; Salaun, M.; Thiberville, L. Classification of Endomicroscopic Images of the Lung Based on Random Subwindows and Extra-Trees. *IEEE Trans. Biomed. Eng.* **2012**, *59*, 2677–2683. [[CrossRef](#)]
31. Chen, S.; Li, X.; Meng, Y.; Xie, Z. Wavelet-based protection strategy for series arc faults interfered by multicomponent noise signals in grid-connected photovoltaic systems. *Solar Energy* **2019**, *183*, 327–336. [[CrossRef](#)]
32. Le, V.; Miller, C.; Tsao, B.; Yao, X. Series Arc Fault Identification in DC Distribution Based on Random Forest Predicted Probability. *IEEE J. Emerg. Sel. Top. Power Electron.* **2023**, *11*, 5636–5648. [[CrossRef](#)]
33. Wang, Z.; Han, C.; Gao, H.; Guo, F. Identification of Series Arc Fault Occurred in the Three-Phase Motor With Frequency Converter Load Circuit via VMD and Entropy-Based Features. *IEEE Sens. J.* **2022**, *22*, 24320–24332. [[CrossRef](#)]
34. Yang, Y.; Huang, L.; Li, P.; Sheng, L.; Lv, Z.; Yang, S. Arc Fault Detection Method Based on Multi-dimension Feature Extraction. *J. Electron. Meas. Instrum.* **2021**, *35*, 107–115.
35. Simonyan, K.; Zisserman, A. Very deep convolutional networks for large-scale image recognition. *arXiv* **2014**, arXiv:1409.1556. [[CrossRef](#)]
36. Li, Y.; Zhang, K.; Cao, J.; Timofte, R.; Van, L. Localvit: Bringing locality to vision transformers. *arXiv* **2021**, arXiv:2104.05707.
37. Sun, Y.; Cao, Y.; Li, P.; Su, S. Fault Diagnosis for RPMs Based on Novel Weighted Multi-Scale Fractional Permutation Entropy Improved by Multi-Scale Algorithm and PSO. *IEEE Trans. Veh. Technol.* **2024**, *73*, 11072–11081. [[CrossRef](#)]
38. Yan, J.; Li, Q.; Duan, S. A Simplified Current Feature Extraction and Deployment Method for DC Series Arc Fault Detection. *IEEE Trans. Ind. Electron.* **2024**, *71*, 625–634. [[CrossRef](#)]
39. Novak, B. *Implementing Arc Detection in Solar Applications: Achieving Compliance with the New UL1699B Standard*; Texas Instruments: Dallas, TX, USA, 2012.

Disclaimer/Publisher's Note: The statements, opinions and data contained in all publications are solely those of the individual author(s) and contributor(s) and not of MDPI and/or the editor(s). MDPI and/or the editor(s) disclaim responsibility for any injury to people or property resulting from any ideas, methods, instructions or products referred to in the content.